A Spectral Analysis of Feedback Regulation near and beyond Nyquist Frequency

Dan Wang, Xu Chen[†]

***Abstract*—A fundamental challenge in sampled-data control arises when a continuous-time plant is subject to disturbances that possess significant frequency components beyond the Nyquist frequency of the feedback sensor. Such intrinsic difficulties create formidable barriers for fast high-performance controls in modern and emerging technologies such as additive manufacturing and vision servo, where the update speed of sensors is low compared to the dynamics of the plant. This paper analyzes spectral properties of closed-loop signals under such scenarios, with a focus on mechatronic systems. We propose a spectral analysis method that provides new understanding of the time- and frequency-domain sampled-data performance. Along the course of uncovering spectral details in such beyond-Nyquist controls, we also report a fundamental understanding on the infeasibility of single-rate high-gain feedback to reject disturbances not only beyond but also below the Nyquist frequency. New metrics and tools are then proposed to systematically quantify the limit of performance. Validation and practical implications of the limitations are provided with experimental case studies performed on a precision mirror galvanometer platform for laser scanning.**

***Index Terms*—Nyquist frequency, feedback regulation, high-gain control, sampled-data control**

I. INTRODUCTION

MANY modern manufacturing systems are increasingly subjected to the challenge of limited sensing in the design of control systems. For instance, in hard disk drive systems, the sampling speed of the closed loop is limited by the amount of physical servo sectors [1], [2]. In selective laser sintering additive manufacturing, infrared thermography cameras are expected to feedback more than 100,000 frames of data every second, which is currently unattainable in a real-time control framework [3], [4]. Similar scenarios also appear in many other systems, such as vision-guided high-speed controls [5], [6] and chemical processes. This paper studies performance of the control system in this important problem space.

The focused feedback system here is a sampled-data one with its fast continuous dynamics controlled by a slow-sampled data feedback. To better motivate the research, we briefly review the existing metrics of sampled-data performance. Let a plant $P_c(s)$ be controlled by a digital controller $C(z)$ under a sampling time T_s (in seconds). It is a standard result from digital control theory that single-rate high-gain control ($|C(\mathrm{e}^{j\Omega_o T_s})| = \infty$) can asymptotically reject disturbances at frequency Ω_o in the *sampled* output. However, for the actual continuous-time output, the situation is more involved. Based on sampled-data control [7]–[11], periodic sampling at T_s partitions the continuous-time frequency into infinite regions of $[2k\pi/T_s, 2(k+1)\pi/T_s)$ where $k = 0, \pm1, \pm2, \dots$, and a continuous-time disturbance yields a fundamental mode plus an infinite number of shifted replicas in the partitioned regions. Due to the sampled-data architecture, the conventional concept of frequency responses does not apply to evaluate the full system performance here [7]–[12]. Three variations are introduced: (i) the fundamental transfer function (FTF) [11], (ii) the performance frequency gain (PFG) [13], [14], and (iii) the robust frequency gain (RFG) [7]. FTF reveals partial information of the full intersample behavior because it focuses only on the fundamental mode. PFG studies the overall sampled-data behavior within certain frequency regions by employing an input-to-output power gain function [15]. RFG forms a metric for robustness by maximizing the input-to-output power ratio over all possible combinations of the magnitudes and phases of the input [16].

Although a sizable literature has studied the generalized frequency responses in sampled-data control, analyses and evaluations for the case with beyond-Nyquist disturbances have not been sufficiently developed. For instance, under a beyond-Nyquist disturbance, PFG and RFG only provide a scalar value as an indicator of the regulation performance. The distribution and closed-loop impact of each sampling-induced alias mode remain not well understood. This can be problematic for control practitioners since it is hard to distinguish whether a spectral peak in the observed output comes from below- or beyond-Nyquist disturbance sources. As will be shown, the spectral effects of high-gain control on beyond-Nyquist disturbances differ greatly from those below π/T_s. This research uncovers the spectral details and, by doing so, reveals the infeasibility of sub-Nyquist high-gain servo design to reject beyond-Nyquist disturbances in mechatronic systems that have low-pass type of dynamics. In particular, we present and validate the existence of an upper frequency bound for rejecting disturbances even *below* the Nyquist frequency. This bound implies a fundamental limitation for high-gain feedback control of sampled-data systems. We provide tools to analyze the limitation and guidance to implement the tools in practical problems. Theoretical analyses in this paper are verified by both simulation and experimentation on a laser scanning platform in additive manufacturing.

The main contributions of the paper are:

- building a full spectral analysis method to evaluate the intersample behavior for beyond-Nyquist disturbances in sampled-data control;
- applying the proposed method to analyze single-rate high-gain control and discovering the existence of a principal

---

The authors are with the Department of Mechanical Engineering, University of Connecticut, Storrs, CT, 06269, USA (emails: `{dan.wang, xchen}@uconn.edu`). [†]: corresponding author.

sampled-data bandwidth B_p below the Nyquist frequency;
- verifying numerically and experimentally the theoretical results in additive manufacturing.

A preliminary version of the findings was presented in [17]. In this paper, we substantially expand the research with new theoretical results and experimental verifications. In the remainder of the paper, Section II reviews several basics of sampled-data control; the main spectral analysis method is provided in Section III; Sections IV and V provide the numerical and experimental verifications of the algorithm, respectively, after which Section VI concludes the paper.

Notations: $x[n]$ and $x_c(t)$ denote, respectively, a discrete sequence and a continuous-time signal. $X(\mathrm{e}^{j\omega})$ denotes the discrete-time Fourier transform (DTFT) of $x[n]$. $X_c(j\Omega)$ is the Fourier transform of $x_c(t)$. $\omega = \Omega T_s$, and Ω is in rad/s.

$\Re(c)$ denotes the real part of a complex number $c \in \mathbb{C}$. For a sampled-data system with measurements collected every T_s sec, single-rate control refers to digital control implemented at the same sampling time of T_s.

II. PRELIMINARIES

Consider the sampled-data control system in Fig. 1, where the solid and the dashed lines represent, respectively, continuous- and discrete-time signal flows. The main elements in the block diagram include the continuous-time plant $P_c(s)$, the analog-to-digital converter (ADC) that samples the continuous output at T_s, the discrete-time controller $C(z)$, and the signal holder $\mathscr{H}$. In this paper, we focus on the case where $\mathscr{H}$ is a zero-order hold (ZOH). The developed tools and analytic framework can be applied to generalized sample hold functions.

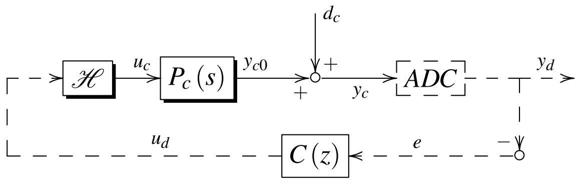

Fig. 1: Block diagram of a sampled-data control system.

Some basic properties and assumptions of sampled-data control are reviewed first for setting up the problem.

It is assumed that 1) $P_c(s) = P_0(s)\mathrm{e}^{-s\tau}$ where $\tau \geq 0$; $P_0(s)$ and $C(z)$ both are LTI, proper, and rational; 2) the coefficients of all transfer functions are real; 3) the closed loop satisfies the *non-pathological sampling condition* [18].

Under assumption 3), the closed-loop sampled-data system is stable if and only if the discrete-time closed loop, consisting of $C(z)$ and the ZOH equivalent of $P_c(s)$, is stable [19], [20].

Lemma 1. [21] If $X_c(j\Omega)$ exists, the sampling process converting $x_c(t)$ to $x[n] = x_c(nT_s)$ gives

$$X\left(\mathrm{e}^{j\omega}\right) = \frac{1}{T_s}\sum_{k=-\infty}^{\infty} X_c\left(j\left(\frac{\omega}{T_s} - \frac{2\pi}{T_s}k\right)\right). \tag{1}$$

Following conventions, we refer to $X_c(j\omega/T_s)$ $(k = 0)$ as the fundamental mode and the other terms $(k \neq 0)$ in the right side of (1) as the shifted replicas.

Because of (1), after d_c passes the ADC and enters the feedback loop, $y_c(t)$ contains a fundamental mode plus an infinite number of aliases:

Lemma 2. [22] If $d_c(t) = \mathrm{e}^{j\Omega_o t}$ and the sampling time is T_s in Fig. 1, then the Fourier transform of the continuous-time plant output $y_c(t)$ is

$$\begin{aligned} Y_c(j\Omega) = {} & 2\pi\left[1 - \frac{1}{T_s}P_c(j\Omega)H(j\Omega)S_d(\mathrm{e}^{j\Omega T_s})C(\mathrm{e}^{j\Omega T_s})\right]\delta(\Omega - \Omega_o) \\ & - \frac{2\pi}{T_s}P_c(j\Omega)H(j\Omega)S_d(\mathrm{e}^{j\Omega T_s})C(\mathrm{e}^{j\Omega T_s}) \sum_{k=-\infty,\ k\neq 0}^{\infty} \delta(\Omega - \Omega_o - \frac{2\pi}{T_s}k), \end{aligned} \tag{2}$$

where $\delta(\Omega - \Omega_o)$ denotes a shifted Dirac delta impulse, $H(j\Omega) = (1 - \mathrm{e}^{-j\Omega T_s})/(j\Omega)$ is the Fourier transform of the ZOH, and $S_d(\mathrm{e}^{j\Omega_o T_s})$ is the frequency response of the discrete-time sensitivity function $S_d(z) = 1/(1 + P_d(z)C(z))$, where $P_d(z)$, the ZOH equivalent of $P_c(s)$, has the DTFT

$$P_d(\mathrm{e}^{j\Omega_o T_s}) = \frac{1}{T_s}\sum_{k=-\infty}^{\infty} P_c(j(\Omega_o + \frac{2\pi}{T_s}k))H(j(\Omega_o + \frac{2\pi}{T_s}k)). \tag{3}$$

In practice, the pure analog output $y_c(t)$ is infeasible to collect and store on digital computers. As an alternative, a fast signal sampled at $T_s^{'}$ is used to approximate the continuous-time output with $T_s^{'} = T_s/F$ ($F > 1$ and $F \in \mathbb{Z}$). The problem then reduces to a multirate (MR) sampled-data control one, as shown in Fig. 2, where the dotted and dashed lines represent the fast and slow signals sampled by $T_s^{'}$ and T_s, respectively.

To reveal the performance of the fast-sampled output y_{dh}, we adopt the PFG metric [13], which considers the power ratio between the input disturbance $d[k] = d(kT_s^{'})$ and the output $y_{dh}[k] = y_{dh}(kT_s^{'})$:

Definition 1. Let $d[k] \in \left\{d[k] : d[k] = c\mathrm{e}^{j\Omega k T_s^{'}}, \|c\|_2 < \infty\right\}$ be applied to an MR system in Fig. 2. The PFG $\mathcal{P}(e^{j\Omega T_s^{'}})$ is defined as

$$\mathcal{P}(e^{j\Omega T_s^{'}}) \triangleq \sup_{d\neq 0} \frac{\|y_{dh}[k]\|_p}{\|d[k]\|_p}, \tag{4}$$

where $\|\cdot\|_p$ represents the discrete-time signal power

$$\|d[k]\|_p \triangleq \sqrt{\lim_{N\to\infty} \frac{1}{2N+1}\sum_{k=-N}^{N} \|d[k]\|^2}, \tag{5}$$

and $\|\cdot\|$ denotes the Euclidean vector norm.

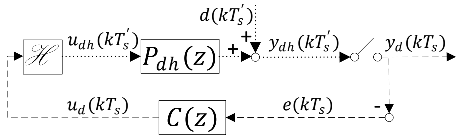

Fig. 2: Block diagram of multirate sampled-data analysis.

III. SPECTRAL ANALYSIS OF BEYOND-NYQUIST REGULATION PROBLEMS

To better motivate the analysis, consider two fast-sampled outputs y_{dh} in Figs. 3 and 4 collected from experimentation on the mirror galvanometer system in Section V. The outputs are fast sampled at $T_s^{'} = T_s/F$ with $F = 4$. The Nyquist frequency is $\Omega_N = 5\,$kHz. The disturbance frequencies are below Ω_N at $3\,$kHz and beyond Ω_N at $7\,$kHz, respectively.

Under a classic PID control design, the two single-harmonic excitations generate aliased modes at multiple frequencies (bottom plots of Figs. 3 and 4). When classic single-rate high-gain control [23] is applied to the feedback system, distinct differences show in the output spectra (top plots of Figs. 3 and 4). Furthermore, all the spectral spikes are not fully attenuated despite the zero steady-state T_s-sampled output (Figs. 7a and 8a). How do the results happen? What is the governing mechanics of the beyond-Nyquist compensation? How would the spectral distribution change with respect to the excitation frequency?

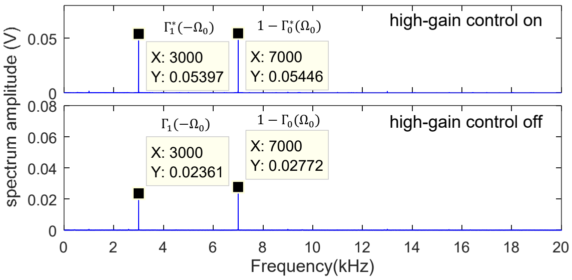

Fig. 3: Fast Fourier transform of $y_{dh}(t)$ with input disturbance frequency at $1.4\Omega_N$.

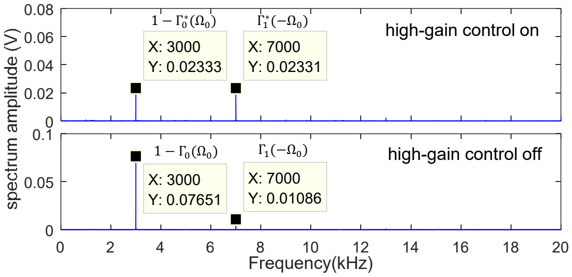

Fig. 4: Fast Fourier transform of $y_{dh}(t)$ with input disturbance frequency at $0.6\Omega_N$.

To decipher the characteristics of the individual frequency spikes, we propose a spectral analysis method integrating the principles of loop shaping, the limiting conditions of high-gain control, and the PFG. For a generalized sampled-data control system in Fig. 1, to determine the magnitudes of the individual spectral spikes, we define the *characteristic feedback loop gain*

$$\Gamma_k(\Omega_o) \triangleq \frac{P_c(j(\Omega_o+\frac{2\pi}{T_s}k))H(j(\Omega_o+\frac{2\pi}{T_s}k))}{T_sP_d(\mathrm{e}^{j\Omega_oT_s})}T_d(\mathrm{e}^{j\Omega_oT_s}), \quad (6)$$

where

$$T_d(\mathrm{e}^{j\Omega_oT_s}) \triangleq \frac{P_d(\mathrm{e}^{j\Omega_oT_s})C(\mathrm{e}^{j\Omega_oT_s})}{1+P_d(\mathrm{e}^{j\Omega_oT_s})C(\mathrm{e}^{j\Omega_oT_s})} = P_d(\mathrm{e}^{j\Omega_oT_s})C(\mathrm{e}^{j\Omega_oT_s})S_d(\mathrm{e}^{j\Omega_oT_s}). \quad (7)$$

After substituting (6) into (2) and recalling that $\mathcal{F}\left\{\mathrm{e}^{j\Omega_0 t}\right\} = 2\pi\delta(\Omega-\Omega_0)$, the steady-state continuous-time output is simplified to

$$y_c(t) = [1-\Gamma_0(\Omega_0)]\mathrm{e}^{j\Omega_0 t} - \sum_{k=-\infty,\ k\neq 0}^{\infty} \Gamma_k(\Omega_0)\mathrm{e}^{j\left(\Omega_0+\frac{2\pi}{T_s}k\right)t}. \quad (8)$$

Fact 1. Based on (3) and (6), it is immediate that

$$\sum_{k=-\infty}^{\infty} \Gamma_k(\Omega_o) = T_d(\mathrm{e}^{j\Omega_oT_s}). \quad (9)$$

For the case of real-valued disturbances in practice, let $d_c(t) = \cos(\Omega_o t+\phi)$. Recall $\cos(\Omega_0 t+\phi) = \Re(\mathrm{e}^{j(\Omega_0 t+\phi)})$, $\mathcal{F}\{\Re(x(t))\} = [\overline{X(-j\Omega)}+X(j\Omega)]/2$, and $\delta(-\Omega-\Omega_o) = \delta(\Omega+\Omega_o)$. Laplace transform to the real part of (8) gives

$$\begin{aligned} Y_c(j\Omega) = {} & \pi\mathrm{e}^{j\phi}(1-\Gamma_0(\Omega_o))\delta(\Omega-\Omega_o) \\ & +\pi\mathrm{e}^{-j\phi}(1-\Gamma_0(-\Omega_o))\delta(\Omega+\Omega_o) \\ & -\pi\mathrm{e}^{j\phi}\sum_{k=-\infty,\ k\neq 0}^{\infty}\Gamma_k(\Omega_0)\delta(\Omega-\Omega_o-\frac{2\pi}{T_s}k) \\ & -\pi\mathrm{e}^{-j\phi}\sum_{k=-\infty,\ k\neq 0}^{\infty}\Gamma_{-k}(-\Omega_0)\delta(\Omega+\Omega_o+\frac{2\pi}{T_s}k). \end{aligned} \quad (10)$$

By the definition in (6), $\underline{\Gamma_k(\Omega_o)}$ is conjugate symmetric, namely, $\Gamma_{-k}(-\Omega_0) = \overline{\Gamma_k(\Omega_0)}$. Thus in (10), the gains for two fundamental modes, $|1-\Gamma_0(\Omega_0)|$ and $|1-\Gamma_0(-\Omega_0)|\left(=\left|\overline{1-\Gamma_0(\Omega_0)}\right|\right)$, are equal, and the gains for their related aliased harmonics, $|\Gamma_k(\Omega_0)|$ and $|\Gamma_{-k}(-\Omega_0)|$, are also equal. The collective effect of these modes governs the dynamics of the output.

It is noteworthy that simultaneously rejecting all modes of $Y_c(j\Omega)$ in (10) is unattainable. Similar to the feedback limitation on simultaneously rejecting disturbances and sensor noises, the gains for the fundamental modes and the aliases cannot be reduced at the same time. For example, letting $C(\mathrm{e}^{j\Omega_oT_s}) = 0$ in (7) yields $\Gamma_k(\Omega_o) = 0$ for any k, namely, a zero gain for each harmonic $|\Gamma_k(\Omega_0)|$ and a unit gain for the fundamental mode $|1-\Gamma_0(\Omega_0)|$ in (10). Thus, perfect "rejection" of the aliased harmonics yields no attenuation of the fundamental disturbance.

To understand the differences in the top plots of Figs. 3 and 4, we explore the shape of the mode gain $\Gamma_k(\Omega_o)$ under high-gain control.

Definition 2. Under ideal single-rate high-gain control, the new characteristic feedback loop gain is

$$\Gamma_k^*(\Omega_o) \triangleq \lim_{|C(\mathrm{e}^{j\Omega_oT_s})|\to\infty} \Gamma_k(\Omega_o) = \frac{P_c(j(\Omega_o+\frac{2\pi}{T_s}k))H(j(\Omega_o+\frac{2\pi}{T_s}k))}{T_sP_d(\mathrm{e}^{j\Omega_oT_s})}. \quad (11)$$

Fact 2. From the definition of $P_d(\mathrm{e}^{j\Omega_oT_s})$ in (3), it is immediate that the summation of $\Gamma_k^*(\Omega_o)$ over k is

$$\sum_{k=-\infty}^{\infty} \Gamma_k^*(\Omega_0) = 1,\ \forall\Omega_0. \quad (12)$$

(12) will be revisited in Section III-B. Similar to $\Gamma_k(\Omega_o)$, $\Gamma_k^*(\Omega_o)$ is also conjugate symmetric: $\left|1-\Gamma_0^*(\Omega_o)\right| = \left|1-\Gamma_0^*(-\Omega_o)\right|$; $\left|\Gamma_k^*(\Omega_o)\right| = \left|\Gamma_{-k}^*(-\Omega_0)\right|$.

A. Characteristic feedback loop gains $\Gamma_k(\Omega_o)$ and $\Gamma_k^*(\Omega_o)$

In this subsection, the properties of the characteristic feedback loop gains are discussed. From (6) and (11), we obtain that $\Gamma_k(\Omega_o) = \Gamma_k^*(\Omega_o)T_d(\mathrm{e}^{j\Omega_oT_s})$. Since $T_d(z)$ is typically a low-pass filter whose bandwidth B_T is commonly 10%-20% of the Nyquist frequency [22], we have $|\Gamma_k^*(\Omega_o)| > |\Gamma_k(\Omega_o)|$ for most frequencies. Furthermore, we can obtain the following characteristics:

1) If $\underline{\Omega_o+2k\pi/T_s \in [0,B_T)}$, then the low-pass $H(j(\Omega_o+2k\pi/T_s))/T_s \approx 1$ in (11). For mechatronic systems

where the plant usually has high gains at low frequencies, $P_c(j(\Omega_o + 2k\pi/T_s))H(j(\Omega_o + 2k\pi/T_s))/T_s \approx P_d(\mathrm{e}^{j(\Omega_o+2k\pi/T_s)T_s}) = P_d(\mathrm{e}^{j\Omega_o T_s})$, and $|T_d(\mathrm{e}^{j\Omega_o T_s})| \approx 1$, yielding both $\Gamma_k(\Omega_o)$ and $\Gamma_k^*(\Omega_o)$ to be approximately 1. Thus, $|1-\Gamma_k(\Omega_o)|$ and $|1-\Gamma_k^*(\Omega_o)|$ are both small. In particular, since $P_d(1) = P_c(0)$ [24] and $H(0)/T_s = 1$, we have $1-\Gamma_0^*(0) = 0$.

2) If $\underline{\Omega_o + 2k\pi/T_s \in [B_T, \pi/T_s)}$, then $|T_d(\mathrm{e}^{j\Omega_o T_s})| < 1$, and thus $|\Gamma_k^*(\Omega_o)| > |\Gamma_k(\Omega_o)|$. For most frequencies in this region, $|\Gamma_k^*(\Omega_o)| \approx 1$, and $|1-\Gamma_k^*(\Omega_o)| \ll 1$.

3) If $\underline{\Omega_o + 2k\pi/T_s \in [\pi/T_s, 2\pi/T_s)}$, the low-pass ZOH $|H(j(\Omega + 2k\pi/T_s))|$ reduces quickly outside its approximate bandwidth π/T_s. Although high-gain control still makes $|\Gamma_k^*(\Omega_o)| > |\Gamma_k(\Omega_o)|$, the overall magnitudes $|\Gamma_k^*(\Omega_o)|$ and $|\Gamma_k(\Omega_o)|$ are very small. Thereby, $\left|1-\Gamma_k^*(\Omega_o)\right|$ and $|1-\Gamma_k(\Omega_o)|$ both approximate 1.

Interestingly, $\Gamma_k^*(\Omega_o)$ has high gains at the Nyquist frequency and its odd multiplications. To see this point, we analyze the property of $|P_d(\mathrm{e}^{j\frac{\pi}{T_s}T_s})| = |P_d(-1)|$ in (11). It is well known that all continuous-time systems with relative degree larger than or equal to two have limiting nonminimum-phase zeros in their ZOH equivalent [24]. In particular, real unstable zeros appear in P_d at high frequencies for small values of T_s. As a result, $|P_d(-1)|$ in (11) is small or even zero, yielding a large $\left|\Gamma_k^*(\frac{\pi}{T_s})\right|$. More specifically, we have the following result:

Lemma 3. If $P_c(s) = 1/s^n$ and n is a positive even integer, then $\Gamma_k^*(\frac{\pi}{T_s}) = \infty$.

Proof: See the Appendix. ■

Lemma 3 illustrates a danger of designing single-rate high-gain controllers near the Nyquist frequency. With the limiting case of $\Gamma_k^*(\frac{\pi}{T_s})$ and $1-\Gamma_k^*(\frac{\pi}{T_s})$ both being infinity, a continuity analysis gives that $\Gamma_k^*(\Omega)$ and $1-\Gamma_k^*(\Omega)$ have very high gains near the Nyquist frequency. Correspondingly, from (10), the continuous-time output is significantly amplified. It is also worth pointing out that the special case of $P_c(s) = 1/s^2$ is common in precision motion control (e.g., in hard disk drives [25] and in wafer scanners used in semiconductor manufacturing).

Fig. 5 illustrates the magnitudes of $\Gamma_k^{(*)}$ and $1-\Gamma_k^{(*)}$ in a motion-control example in Section IV. The Nyquist frequency is indicated by the vertical line at π/T_s. The shapes of the curves match well with the above analysis. As an analysis tool, Fig. 5 reveals several fundamental performance limitations of single-rate high-gain control:

- *First*, based on the top plot in Fig. 5, unless at very low frequencies (below B_T) where $\Gamma_k(\Omega) \approx \Gamma_k^*(\Omega)$, the aliased harmonics are all amplified by single-rate high-gain control.
- *Second*, high-gain control in $C(z)$ only provides enhanced rejection of the *fundamental* disturbance mode below the intersection frequency of $|1-\Gamma_0^*(\Omega)|$ and $|1-\Gamma_0(\Omega)|$ (B_c in Fig. 5). In addition, the achievable maximum attenuation—indicated by the magnitude $|1-\Gamma_0^*(\Omega)|$—decreases with increasing frequency. For common servo design with low-pass type of complementary sensitivity functions T_d, the first two points suggest that single-rate high-gain control *cannot reject continuous-time disturbances near and above Nyquist frequency*.
- *Third*, for $\Omega_o \in (\pi/T_s, 2\pi/T_s)$, $|\Gamma_k^*(\Omega_o)| > |\Gamma_k(\Omega_o)|$, and $|1-\Gamma_0^*(\Omega_o)| \gtrsim |1-\Gamma_0(\Omega_o)| \approx 1$. In this interval, under single-rate high-gain control, Ω_o being closer to π/T_s causes larger servo degradation, which is different from classic servo control where disturbances at lower frequencies are commonly easier to be attenuated.

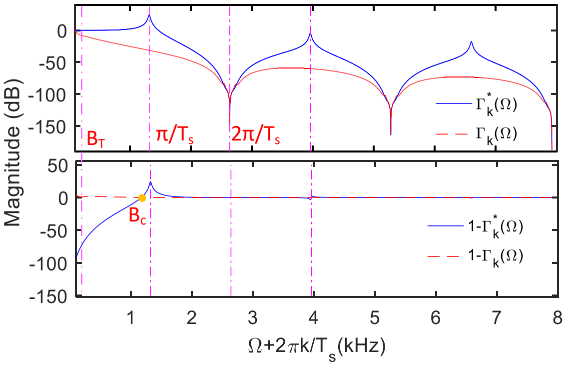

Fig. 5: Magnitude responses of $\Gamma_k(\Omega)$, $\Gamma_k^*(\Omega)$, $1-\Gamma_k(\Omega)$ and $1-\Gamma_k^*(\Omega)$ as a function of $\Omega + 2\pi k/T_s$, where $\Gamma_k^*(\Omega_o)$ and $\Gamma_k(\Omega_o)$ denote the characteristic feedback loop gain with and without high-gain control respectively. The first three vertical lines indicate, respectively, the Nyquist frequency, the sampling frequency and $3/2T_s$.

Remark 1. For implementation, it is noteworthy that with the low-pass dynamics in ZOH, the first few frequency modes in (10) are usually dominant in magnitude. In Fig. 5, after $3 \cdot \frac{2\pi}{T_s}$, the magnitudes of $\Gamma_k(\Omega)$ and $\Gamma_k^*(\Omega)$ are relatively insignificant, and $\left|1-\Gamma_k^{(*)}(\Omega)\right|$ is practically equal to 1.

B. Typical spectrum of $y_c(t)$ in sampled-data control

In this subsection, we extend the analysis and study the full beyond-Nyquist spectra of the output signals.

Let $\Omega_o \in (\pi/T_s, 2\pi/T_s)$ and $\Omega_o' = 2\pi/T_s - \Omega_o \in (0, \pi/T_s)$. Consider two different disturbances $d_c(t) \triangleq \cos(\Omega_o t)$ and $\tilde{d}_c(t) \triangleq \cos(\Omega_o' t)$, respectively, at above and below the Nyquist frequency. The Fourier transforms of the continuous-time disturbances are

$$D_c(j\Omega) = \pi\delta(\Omega - \Omega_o) + \pi\delta(\Omega + \Omega_o),$$
$$\tilde{D}_c(j\Omega) = \pi\delta(\Omega - \Omega_o - \frac{2\pi}{T_s}) + \pi\delta(\Omega + \Omega_o - \frac{2\pi}{T_s}).$$

From (1), the sampled disturbance spectra and hence $y_d[k]$ are the same. However, the spectra of $y_c(t)$ are fundamentally different for the two types of disturbances, as illustrated in Figs. 6a and 6c. One important difference is the location of the fundamental mode (Ω_o for d_c and $2\pi - \Omega_o$ for $d_c^{'}$). For Ω_o being above Nyquist frequency, the magnitude of the fundamental mode $|1-\Gamma_0(\Omega_o)|$ is close to 1 (cf. Fig. 5). The dominant aliased mode $\Gamma_1(-\Omega_o)$ occurs at $2\pi/T_s - \Omega_o$ below the Nyquist frequency (see Fig. 6a). With single-rate high-gain control at Ω_o, the magnitude of $\Gamma_k(\Omega_o)$ increases towards the limiting case $\Gamma_k^*(\Omega_o)$. In particular, $\Gamma_1(-\Omega_o)$ increases towards $\Gamma_1^*(-\Omega_o) \approx 1$ (Fig. 6b). Meanwhile, $|1-\Gamma_k(\Omega_o)|$ stays close to 1 or is even increased. Collectively, $d_c(t)$ is amplified by single-rate high-gain control.

On the other hand, for Ω_o' below the Nyquist frequency, the fundamental mode $1-\Gamma_0(\Omega_o^{'})$ can be effectively reduced (from the dashed line to the solid line in the bottom plot of Fig. 5). The aliased modes $\Gamma_k(\Omega_o')$ still increase to $\Gamma_k^*(\Omega_o')$. However, $|\Gamma_k^*(\Omega_o^{'})|$ remains small in the top plot of Fig. 5 since the lowest frequency of the alias is already beyond the Nyquist frequency (at $2\pi/T_s-\Omega_o^{'}$). Thus, $\tilde{d}_c(t)$ can be reduced by single-rate high-gain control.

The graphical tool is justified by the experimental results in Figs. 3 and 4. In Fig. 3, the fundamental mode occurs at 7000 Hz, and the amplified mode at 3000 Hz corresponds to the alias mode below the Nyquist frequency. In Fig. 4, the frequencies of the two modes are switched. We can now distinguish that Fig. 3 describes the trend of the case in Figs. 6a and 6b while Fig. 4 matches the results in Figs. 6c and 6d.

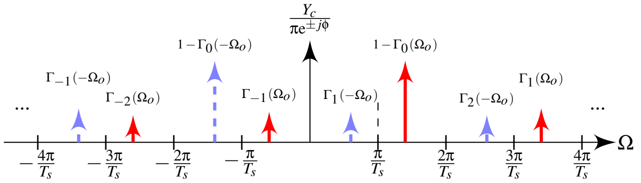

(a) $d_c(t)=\cos(\Omega_o t)$ with the baseline control

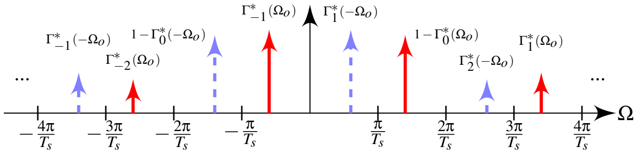

(b) $d_c(t)=\cos(\Omega_o t)$ with enhanced discrete-time high-gain control at Ω_o

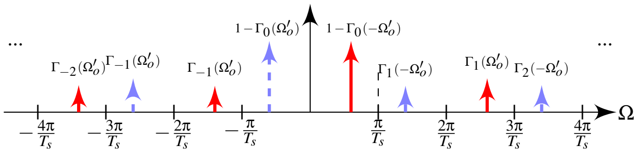

(c) $\tilde{d}_c(t)=\cos(\Omega_o' t)=\cos((2\pi/T_s-\Omega_o)t)$ with the baseline control

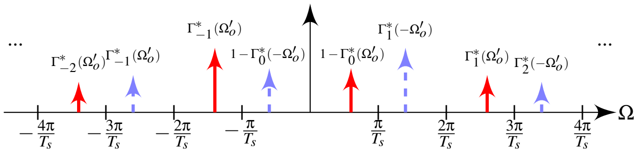

(d) $\tilde{d}_c(t)=\cos(\Omega_o' t)$ with enhanced discrete-time high-gain control at Ω_o

Fig. 6: Illustration of the spectrum of $y_c(t)$ in sampled-data control when $\pi/T_s<\Omega_o<2\pi/T_s$. Dashed spikes: $\delta(\Omega+\Omega_0)$ and its aliases; solid spikes: $\delta(\Omega-\Omega_0)$ and its aliases.

Next we show how to *connect the frequency-domain results with the time-domain observations*. With sub-Nyquist high-gain control, the T_s-sampled disturbances $d_c(t)$ and $\tilde{d}_c(t)$ can be perfectly rejected from the sampled output, as shown in the corresponding time-domain responses of Figs. 7a and 8a. The disturbance rejection may conventionally suggest null gains in the spectrum below the Nyquist frequency, which is, however, neither the case for $d_c(t)$ or $\tilde{d}_c(t)$. In fact, Fig. 6b contains significant components at $2\pi/T_s-\Omega_o$. And Fig. 7b shows the hidden amplification of the disturbances. To connect the spectral distribution with the zero steady-state T_s-sampled output, an important piece is the effect of the sampling operation in the frequency domain. Take the case of $d_c(t)$ as example. After $y_c(t)$ is sampled at T_s, each solid spike in Fig. 6b creates an alias at Ω_o (cf. Lemma 1). Based on (10), the magnitude of the discrete-time spectral peak at Ω_0 is a normalized version of $[1-\Gamma_o^*(\Omega_o)]-\Gamma_{-1}^*(\Omega_o)-\Gamma_1^*(\Omega_o)-\Gamma_{-2}^*(\Omega_o)-\Gamma_2^*(\Omega_o)-\dots$, which equals 0 from (12). For the case where the disturbance is beyond Nyquist frequency in Fig. 6b, because there is little control over $1-\Gamma_0(\Omega_o)$, and $\Gamma_{\pm k}(\Omega_o)$ $(k\neq 0)$ is amplified, the aliasing effect cancels the fundamental component after sampling. Fig. 6d, on the other hand, achieves zero T_s-sampled output by reducing the magnitude of $1-\Gamma_0(\Omega_o')$.

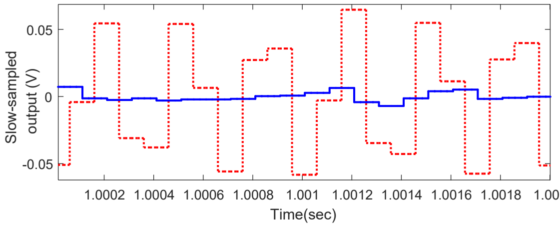

(a) $y_d(t)$ with the sampling time of T_s.

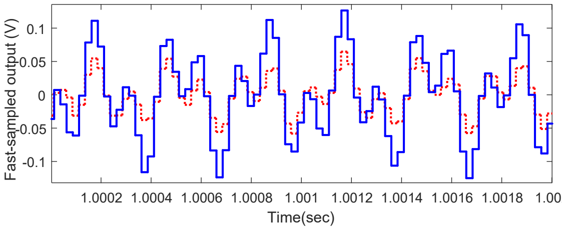

(b) $y_{dh}(t)$ with the sampling time of $T_s^{'}$.

Fig. 7: Plant output with the input disturbance at $1.4\Omega_N$ (*The solid and dashed lines represent the cases with single-rate high-gain control on and off, respectively.*)

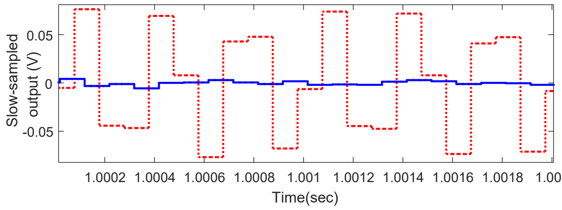

(a) $y_d(t)$ with the sampling time of T_s.

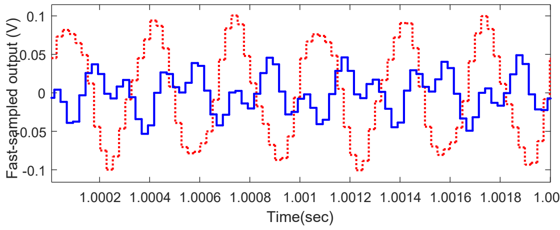

(b) $y_{dh}(t)$ with the sampling time of $T_s^{'}$.

Fig. 8: Plant output with the input disturbance at $0.6\Omega_N$ (*The solid and dashed lines represent the cases with single-rate high-gain control on and off, respectively.*)

C. Performance frequency gain and the fundamental mode

With the understanding of individual mode shapes, we can better relate the spectral responses to the time-domain data in sampled-data control and explain the beyond-Nyquist disturbance rejection. This section connects the analysis of the individual modes with the PFG metric. An important observation is that under single-rate high-gain control, PFG also has a high gain near the Nyquist frequency.

Recall the transformation of a sampled-data system into an MR one by fast sampling in Fig. 2. The fast and slow signals are sampled by $T_s^{'}$ and $T_s = FT_s^{'}$, respectively. Let $D(\mathrm{e}^{j\Omega T_s^{'}})$ denote the DTFT of $d[k]$. Analogous to the derivation of (2), the DTFT of the fast-sampled output $y_{dh}[k]$ [15] is

$$\begin{aligned}Y_{dh}(\mathrm{e}^{j\Omega T_s^{'}}) = &\left[1-\frac{1}{F}P_{dh}(\mathrm{e}^{j\Omega T_s^{'}})H(\mathrm{e}^{j\Omega T_s^{'}})T_d(\mathrm{e}^{j\Omega T_s})/P_d(\mathrm{e}^{j\Omega T_s})\right]D(\mathrm{e}^{j\Omega T_s^{'}})\\ &+\frac{1}{F}P_{dh}(\mathrm{e}^{j\Omega T_s^{'}})H(\mathrm{e}^{j\Omega T_s^{'}})T_d(\mathrm{e}^{j\Omega T_s})/P_d(\mathrm{e}^{j\Omega T_s})\sum_{k=1}^{F-1}D(\mathrm{e}^{j(\Omega T_s^{'}-\frac{2\pi k}{F})}),\end{aligned}\tag{13}$$

where P_d and P_{dh} represent the ZOH plant models under the sampling time of T_s and $T_s^{'}$, respectively, and the transfer function of the ZOH interpolator is

$$H(z)=\sum_{k=0}^{F-1}z^{-k}=\begin{cases}F & z=1\\ \frac{1-z^{-F}}{1-z^{-1}} & z\neq 1\end{cases}.\tag{14}$$

Based on (13), the MR characteristic feedback loop gain is defined as

$$\Gamma_k(\Omega_o)=\frac{P_{dh}(\mathrm{e}^{j(\Omega_o T_s^{'}+\frac{2\pi k}{F})})H(\mathrm{e}^{j(\Omega_o T_s^{'}+\frac{2\pi k}{F})})T_d(\mathrm{e}^{j\Omega_0 T_s})}{FP_d(\mathrm{e}^{j\Omega_0 T_s})},\tag{15}$$

and the limiting case with single-rate high-gain control is

$$\Gamma_k^{*}(\Omega_o)=\frac{P_{dh}(\mathrm{e}^{j(\Omega_o T_s^{'}+\frac{2\pi k}{F})})H(\mathrm{e}^{j(\Omega_o T_s^{'}+\frac{2\pi k}{F})})}{FP_d(\mathrm{e}^{j\Omega_0 T_s})}.\tag{16}$$

Lemma 4. For the MR system in Fig. 2, the modified PFG under single-rate high-gain control at Ω_0 is

$$\mathcal{P}_h(\mathrm{e}^{j\Omega_0 T_s^{'}})=\sqrt{\left\|1-\Gamma_0^{*}(\Omega_o)\right\|^2+\sum_{k=1}^{F-1}\left\|\Gamma_k^{*}(\Omega_o)\right\|^2}.\tag{17}$$

The derivation is similar to the one introduced in [15] and is omitted here. Lemma 4 connects the input-output power ratio with the gains of the individual signal modes. PFG evaluates the overall effect of the intersample behavior and how a sampled-data control system attenuates or amplifies input disturbances in certain frequencies, whereas the characteristic feedback loop gains look into each individual mode in the spectra of the continuous-time (and fast-sampled) outputs.

Note that independent of the baseline controller, the modified PFG is a property of the plant itself since $\Gamma_k^{*}(\Omega_o)$ depends on P_{dh}, H, F, and P_d alone. In addition, the modified PFG is a pointwise quantity that focuses on the limiting case where ideal high-gain control is applied at one value of Ω_0, that is, $T_d(\mathrm{e}^{j\Omega_o T_s})=1$. This pointwise high-gain control can be achieved with tools such as special Youla-Kucera parameterizations, disturbance observers, and peak filters [23], [26], [27]. To introduce $T_d(\mathrm{e}^{j\Omega_o T_s})=1$ at different values of Ω_0, the high-gain controller would need to be retuned or be adaptive. When the customized high-gain control is turned off, the high-gain controller is replaced by a regular servo algorithm (e.g. PID and lead-lag compensation), and therefore $\Gamma_0^{*}(\Omega_o)$ and $\Gamma_k^{*}(\Omega_o)$ are replaced by $\Gamma_0(\Omega_o)$ and $\Gamma_k(\Omega_o)$ in (15). The modified PFG then describes the performance of a baseline LTI controller.

For a typical plant dynamic in Section V, $\mathcal{P}_h(\mathrm{e}^{j\Omega T_s^{'}})$ is calculated and plotted in Fig. 9.

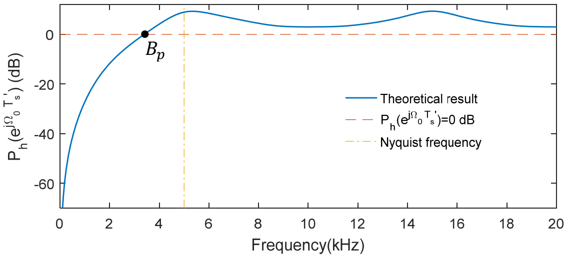

Fig. 9: Performance frequency gain under high-gain control.

Definition 3. The intersection frequency between the curve expressed by (17) and the line of $\mathcal{P}_h(\mathrm{e}^{j\Omega T_s^{'}})=0$ dB is called the *principal sampled-data bandwidth B_p*.

Lemma 5. For general mechatronic systems, B_p is smaller than the Nyquist frequency.

Proof: See the Appendix. ■

Implications: Similar to the analyses of the discrete-time sensitivity function in digital control, the proposed PFG analysis gives an important threshold frequency B_p in sampled-data control. For disturbance frequencies below B_p, the power of the fast-sampled output signal is smaller than that of the input disturbance. In other words, sub-Nyquist high-gain control is efficient for rejecting disturbances with frequencies below B_p. However, for beyond-B_p disturbances with $\mathcal{P}_h > 0\,\mathrm{dB}$, single-rate high-gain control exacerbates the servo performance.

Remark 2. In practice, disturbances can also enter from the input of the plant in Fig. 2. In this case, the input disturbance d_i is related to d in Fig. 2 by $D(\mathrm{e}^{j\Omega T_s^{'}})=D_i(\mathrm{e}^{j\Omega T_s^{'}})P_{dh}(\mathrm{e}^{j\Omega T_s^{'}})$. We can analogously define and compute the modified input PFGs

$$\mathcal{P}_b^{'}(\mathrm{e}^{j\Omega_0 T_s^{'}})=\sup_{d_i\neq 0}\frac{\|y_{dh}\|_p}{\|d_i\|_p}=\left|P_{dh}(\mathrm{e}^{j\Omega_0 T_s^{'}})\right|\sqrt{\|1-\Gamma_0(\Omega_o)\|^2+\sum_{k=1}^{F-1}\|\Gamma_k(\Omega_o)\|^2},\tag{18}$$

and

$$\mathcal{P}_h^{'}(\mathrm{e}^{j\Omega_0 T_s^{'}})=\lim_{T_d(\mathrm{e}^{j\Omega_0 T_s^{'}})\to 1}\mathcal{P}_b^{'}(\mathrm{e}^{j\Omega_0 T_s^{'}})=|P_{dh}|\sqrt{\|1-\Gamma_0^{*}(\Omega_o)\|^2+\sum_{k=1}^{F-1}\left\|\Gamma_k^{*}(\Omega_o)\right\|^2}.\tag{19}$$

The modified input PFG can be verified by the time-domain definition in (18), that is, dividing output signal power by input signal power. Dividing the modified input PFG $\mathcal{P}_h^{'}(\mathrm{e}^{j\Omega_0 T_s^{'}})$ by $\left|P_{dh}(\mathrm{e}^{j\Omega_0 T_s^{'}})\right|$, we can then generate the modified PFG $\mathcal{P}_h(\mathrm{e}^{j\Omega_0 T_s^{'}})$.

Before presenting the numerical and experimental results, we briefly summarize the application steps of the proposed spectral analysis method:

1) Determine $\Gamma_k(\Omega_o)$, the characteristic feedback loop gains, by (6) and (15). In addition, determine $\Gamma_k^{*}(\Omega_o)$, the limiting cases with single-rate high-gain control, by (11) and (16).

2) Plot the magnitude responses of $\Gamma_k(\Omega)$, $\Gamma_k^*(\Omega)$, $1-\Gamma_k(\Omega)$, and $1-\Gamma_k^*(\Omega)$ to look into individual spectral spikes. Note that these are hybrid functions of continuous- and discrete-time frequency responses.
3) Calculate and plot the modified PFG based on (17).
4) Identify the principal sampled-data bandwidth B_p, as shown in Fig. 9.
5) Run simulation and experimentation to get the time- and frequency-domain results with below- and beyond-B_p disturbance input. Numerically compute the modified PFG from the input-to-output power ratio in Definition 1. The results should verify the location of B_p and the trend of the individual spectral spikes.

IV. NUMERICAL VERIFICATION

Consider a plant $P_c(s) = 3.74488 \times 10^9/(s^2 + 565.5s + 319775.2)$ with an input delay of $10\,\mu$s. Let the sampling time be $T_s = 1/2640$ sec. The baseline controller is a PID controller $C(z) = k_p + k_i/(z-1) + k_d(z-1)/z$ with $k_p = 7.51 \times 10^{-5}$, $k_i = 3.00 \times 10^{-5}$, and $k_d = 3.60 \times 10^{-4}$. Such a design provides a bandwidth at 92 Hz that complies with the rule-of-thumb of around 10% of the Nyquist frequency. $y_c(t)$ is fast-sampled at $T_s^{'} = T_s/20$ to approximate the continuous-time output in Fig. 1. Single-frequency vibrations below and above the Nyquist frequency are introduced to the plant. The narrow-band disturbance observer (DOB) [23] is applied on top of the PID controller. Such a design provides perfect compensation of above- and below-Nyquist sinusoidal signals in the *sampled* output $y_d[k]$.

Figs. 10 and 11 present the time- and frequency-domain computation results, which verify the limitation of single-rate high-gain control for beyond-Nyquist disturbance rejection. The results match with the prediction in Fig. 6 that single-rate high-gain control amplifies beyond-Nyquist disturbances. When the disturbance occurs at 2376 Hz ($1.8\Omega_N$), the inter-sample signal is significantly amplified in Fig. 10b, although high-gain control yields zero sampled-output at steady state (Fig. 10a). The amplification is also evident in the frequency domain (Fig. 11). Single-rate high-gain control barely changes the fundamental component at 2376 Hz but greatly amplifies the aliased component at 264 Hz.

Fig. 12 verifies the case with regular below-Nyquist disturbances. The T_s-sampled output also reaches zero at steady state and is omitted here. With the fundamental mode at 924 Hz (below the Nyquist frequency), single-rate high-gain control can attenuate this spectral spike. As theoretically predicted by Fig. 6d, the aliased harmonics are, however, all amplified. Therefore, the actual continuous-time output contains inter-sample ripples.

V. EXPERIMENTAL VERIFICATION

Experiments are conducted on a galvo scanner platform (Fig. 13), a key component in laser-based additive manufacturing. Typically, a galvo scanner is composed of mirrors, galvanometers, and control systems. The mirrors are actuated to reflect the input laser beam to generate a scanning trajectory at high speed with high precision. The angular rotation of the mirrors are measured by encoders.

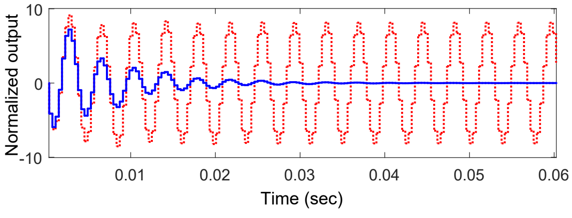

(a) $y_c(t)$ sampled at T_s.

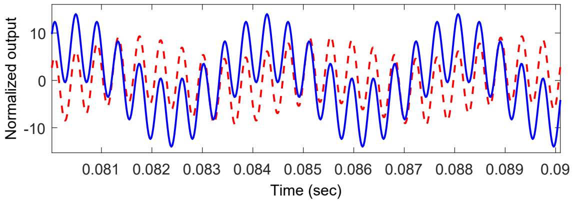

(b) $y_c(t)$ sampled at $T_s/20$.

Fig. 10: Plant output with the input disturbance at $1.8\Omega_N$ (*The solid and dashed lines represent the cases with single-rate h*

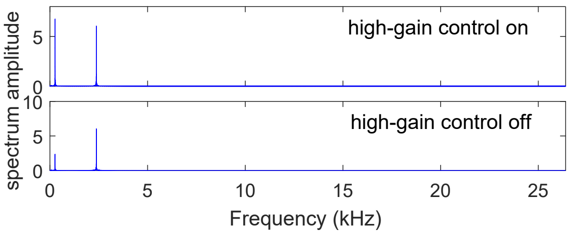

Fig. 11: Fast Fourier transform of $y_c(t)$ sampled at $T_s/20$.

To form a baseline servo system, a built-in PID-type controller $C_0(z)$ is embedded in the motor driver. $C_0(z)$ and the actual plant $P_0(z)$ are treated as the new plant $P_{dh}(z)$ in this study. Fig. 14 shows the frequency response of the measured and identified $P_{dh}(z)$. The DOB [23] with $C(z) = 1$ in Fig. 15 is implemented on a dSPACE DS1104 processor board to enable high-gain control at selective frequencies. Transfer functions inside the DOB block are all implemented at a sampling time of $T_s = 0.1\,$ms. Thus the Nyquist frequency Ω_N equals 5 kHz. The fundamental sampling time used to measure y_{dh} is $T_s^{'} = 0.025\,$ms. That is, the fast sampling is conducted at $T_s^{'} = T/F$ with $F = 4$ for diagnosis of the beyond-Nyquist performance. A single-harmonic disturbance with magnitude 0.1V and frequency $\omega_o = 2\pi\Omega_o T_s^{'}$ (Ω_o in Hz) is introduced to the system. In addition, the system is subjected to broadband random disturbances at a magnitude of about 20 mV.

Fig. 16 illustrates the theoretically computed input PFGs using (18) for the baseline controller and (19) for the customized high-gain controller. Experimental data of $\mathcal{P}_h^{'}(\mathrm{e}^{j\Omega_0 T_s^{'}})$ is obtained by following the time-domain definition in (18) for each value of Ω_o. From Fig. 16, the three experimental PFGs of $\mathcal{P}_h^{'}(\mathrm{e}^{j\Omega_0 T_s^{'}})$ at 3 kHz ($0.6\Omega_N$), 4 kHz (0.8Ω), and 7 kHz ($1.4\Omega_N$) match the theoretical computations very well.

As stated in Remark 2, $\mathcal{P}_h(\mathrm{e}^{j\Omega_0 T_s^{'}})$ is obtained by means of dividing $\mathcal{P}_h^{'}(\mathrm{e}^{j\Omega_0 T_s^{'}})$ by $\left|P_{dh}(\mathrm{e}^{j\Omega_0 T_s^{'}})\right|$. Three groups of validations for $\mathcal{P}_h(\mathrm{e}^{j\Omega_0 T_s^{'}})$ are shown in Table I and Fig. 17. The results show that the mismatch between the experimental and theoretical values is very small, and thus the modified PFG

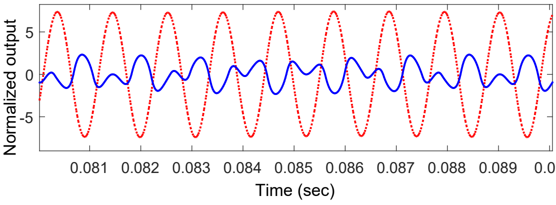

(a) $y_c(t)$ sampled at $T_s/20$. (*The solid and dashed lines represent the*

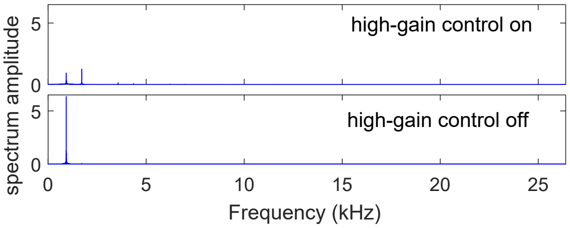

(b) Fast Fourier transform of $y_c(t)$ sampled at $T_s/20$.

Fig. 12: Plant output with the input disturbance at $0.7\Omega_N$

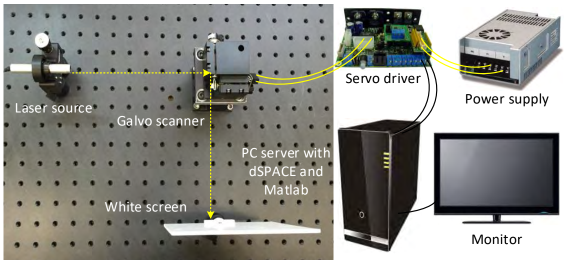

Fig. 13: Schematic of the hardware platform.

is an efficient tool for evaluating the intersample behavior. One principal reason for the mismatch is that in Definition 1, PFG is evaluated according to $N \to \infty$, while only a finite duration of the signal can be reached in experiments.

Disturbance frequency	Group	Experimental PFGs (dB)	Average	Theoretical PFGs
3 kHz	G1 G2 G3	-1.189 -0.961 -0.949	-1.033 dB	-2.847 dB
4 kHz	G1 G2 G3	5.481 5.999 6.258	5.913 dB	4.135 dB
7 kHz	G1 G2 G3	6.023 6.357 6.345	6.242 dB	6.374 dB

TABLE I: Experimental results of the modified PFG.

We have already seen the different cases of time-domain responses in Figs. 7 and 8. Additionally, Fig. 19 verifies the performance limitation for disturbances even below the Nyquist frequency. From the slow-sampled data in Figs. 7a, 8a, and 19a, the single-rate DOB is successful in "compensating" the sampled output. However, similar as the case in the previous numerical study, the hidden performance loss for the case with beyond- and *near*-Nyquist disturbances is obvious from Figs. 7b and 19b.

Fortunately, these performance differences can be predicted by the modified PFG in Fig. 17 and the characteristic feedback loop gains in Fig. 18. The PFG plots predict that high-gain control results in decreased output power for the disturbance at 3 kHz and increased output energy for the disturbances at 4 kHz and 7 kHz. Fig. 18 additionally reveals that both the fundamental and aliased mode gains are increased when disturbances occur at 4 kHz and 7 kHz.

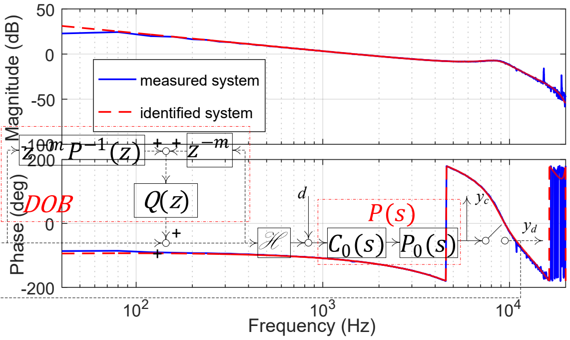

Fig. 14: Bode plot of $P_{dh}(z)$ sampled at T_s'.

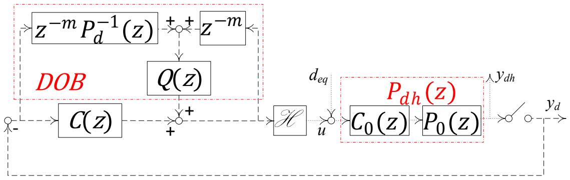

Fig. 15: Block diagram with a disturbance observer (DOB).

The experimental result in Fig. 3 verifies that for the input disturbance with $\Omega_o = 1.4\Omega_N = 7$ kHz, the fundamental component at 7 kHz and the aliased harmonic at 3 kHz are amplified when customized single-rate high-gain control is turned on. For the case with $\Omega_o = 0.8\Omega_N = 4$ kHz, the magnitude of the fundamental mode at 4 kHz barely changes, but the aliased harmonic at 6 kHz is amplified by sub-Nyquist high-gain control, resulting in the overall amplification. For $\Omega_o = 0.6\Omega_N = 3$ kHz, $|1-\Gamma_0^*(\Omega_o)| < |1-\Gamma_0(\Omega_o)|$, and $|\Gamma_1^*(-\Omega_o)| > |\Gamma_1(-\Omega_o)|$; although the aliased mode at 7 kHz is slightly amplified, the attenuation of the fundamental mode at 3 kHz is significant (Fig. 4), resulting in the overall attenuation.

In summary, we experimentally verified that the characteristic feedback loop gains, along with the modified PFG, are reliable tools for analyzing servo performance in sampled-data control. Single-rate high-gain control is observed to amplify all beyond-Nyquist and even some below-Nyquist disturbances.

VI. CONCLUSION AND DISCUSSIONS

In this paper, the problem of sampled-data regulation control against structured disturbances around and beyond the Nyquist frequency is analyzed. It is shown that the conventional sub-Nyquist single-rate high-gain control is infeasible to attenuate disturbances near and beyond the Nyquist frequency. We discover an intersection frequency defined as the principal sampled-data bandwidth B_p. Only for below-B_p disturbances can single-rate high-gain control be effective in disturbance rejection. A spectral analysis is further proposed to look into individual spectral modes. The proposed characteristic feedback loop gains are combined with the performance frequency gain to evaluate the overall sampled-data performance. The results imply that the rejection of beyond-Nyquist vibration disturbances must rely on tools that can facilitate the inter-sample attenuation, such as customized multirate control [28],

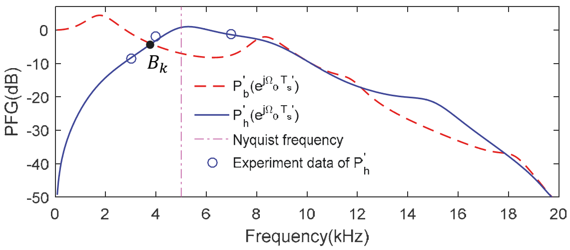

Fig. 16: Input performance frequency gains (PFGs) with high-gain control on and off.

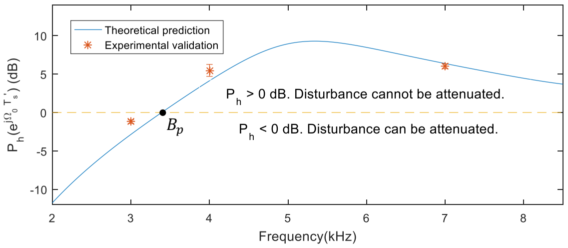

Fig. 17: Theoretical and experimental PFGs.

sampled-data internal model principle [29], sampled-data LQG [30], sampled-data all-stabilizing control [31], and sampled-data H_∞ theory (see [32] and the references therein). For potential future work, the proposed study may have synergy with the analysis and design of nonlinear systems in the frequency domain (e.g., [33]–[35]).

VII. APPENDIX: PROOFS

Proof of Lemma 3

Proof: Recall $\mathcal{L}^{-1}\{P_c(s)/s\}=t^n/(n!)$ by the inverse Laplace transform. Thus, the ZOH equivalent of $P_c(s)$ is

$$P_d(z)=(1-z^{-1})\mathcal{Z}\left\{\frac{(kT_s)^n}{n!}\right\}=\frac{T_s^n(1-z^{-1})}{n!}\sum_{k=0}^{\infty}k^n z^{-k}. \quad (20)$$

We adopt two fundamental functions in number theory to evaluate $P_d(z)$ at $z=-1$. Notice that $\sum_{k=0}^{\infty}k^n(-1)^{-k}=-\eta(-n)=-(1-2^{1+n})\zeta(-n)$, where $\eta(n)$ is the Dirichlet Eta Function and $\zeta(n)$ is the Riemann Zeta Function [36] defined by

$$\zeta(n)\triangleq\begin{cases}\sum_{k=1}^{\infty}\frac{1}{k^n}, & \Re\{n\}>1\\ (1-2^{1-n})^{-1}\sum_{k=1}^{\infty}\frac{(-1)^{k-1}}{k^n}, & \Re\{n\}>0\end{cases}.$$

$\zeta(n)$ is furthermore extended to the whole complex plane by analytic continuation and satisfies the functional equation [37], [38, Chapter 2]

$$\zeta(-n)=2^{-n}\pi^{-n-1}\sin\left(-\frac{\pi n}{2}\right)\overline{\Gamma}(1+n)\zeta(1+n), \quad (21)$$

where $\overline{\Gamma}(n)$ is the Gamma function and $n\in\mathbb{C}$. From the factor $\sin\left(-\frac{\pi n}{2}\right)$, $\zeta(-n)$ has zeros at all positive even integers of n (called the "trivial zeros"). Hence after substitution into (20), $P_d(-1)=0$ when n is a positive even integer. By definition,

$$P_c(j(\Omega_o+\frac{2\pi}{T_s}k))H(j(\Omega_o+\frac{2\pi}{T_s}k))=\frac{1-e^{-j(\Omega_o+\frac{2\pi}{T_s}k)T_s}}{j^{n+1}(\Omega_o+\frac{2\pi}{T_s}k)^{n+1}},$$

which is finite when $\Omega_o=\pi/T_s$. Hence Lemma 3 holds. ■

Remark 3. A numerical evaluation of the zeta function is available at [39]. The ZOH equivalents of $1/s^n$ for n up to 8 are numerically evaluated in [24]. There, a zero at -1 is evident for $n=2,4,6,8$.

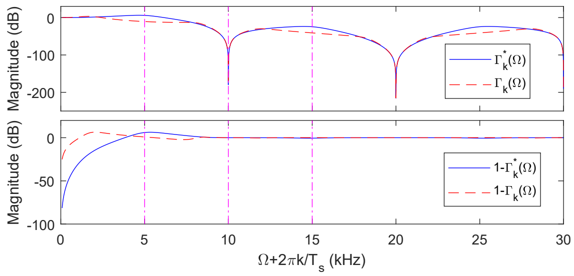

Fig. 18: Magnitude responses of $\Gamma_k(\Omega)$, $\Gamma_k^*(\Omega)$, $1-\Gamma_k(\Omega)$ and $1-\Gamma_k^*(\Omega)$ as a function of $\Omega+2\pi k/T_s$. The first three vertical lines indicate, respectively, the Nyquist frequency (5 kHz), the sampling frequency and $3/2T_s$.

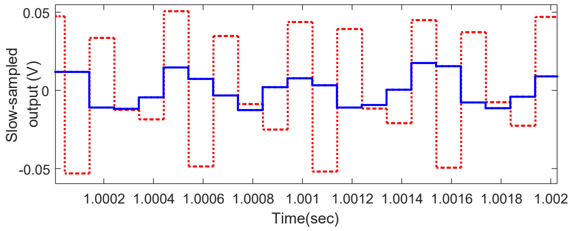

(a) $y_d(t)$ with the sampling time of T_s.

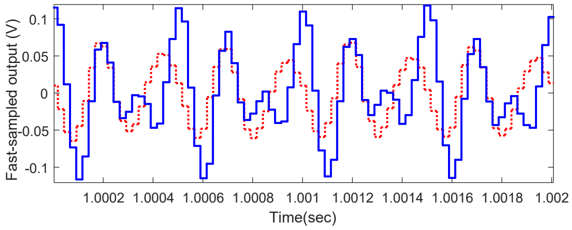

(b) $y_{dh}(t)$ with the sampling time of $T_s^{'}$.

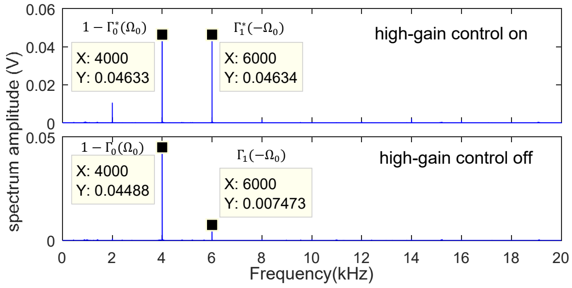

(c) Fast Fourier transform of $y_{dh}(t)$.

Fig. 19: Plant output with the input disturbance at $0.8\Omega_N$ (*For (a) and (b), the solid and dashed lines represent the cases with single-rate high-gain control on and off, respectively.*)

Proof of Lemma 5

Proof: Take an inertia system $P_c(s)=1/s^2$ in motion control as example.[1] We show that $\mathcal{P}_h(e^{j\cdot 0\cdot T_s^{'}})<1$ and $\mathcal{P}_h(e^{j\Omega_N T_s^{'}})>1$. If PFG is a continuous function of Ω_o for $\Omega_o\in(0,\Omega_N)$, $\mathcal{P}_h(e^{j\Omega_0 T_s^{'}})$ then must cross over the 0 dB line at least once below the Nyquist frequency Ω_N. In other words, under the metric of PFG, it is inevitable that some band-limited

---

[1] Without loss of generality, the gain of $P_c(s)$ is normalized to unity. Non-unity gains are canceled in the computation of $\Gamma_k(\Omega_o)$ and $\Gamma_k^*(\Omega_o)$ in (16).

disturbances below the Nyquist frequency are amplified by single-rate high-gain control.

With $P_c(s) = 1/s^2$, we have $P_d(z) = T_s^2(z+1)/\left[2(z-1)^2\right]$ and $P_{dh}(z) = T_s^{\prime 2}(z+1)/\left[2(z-1)^2\right]$. When $\Omega_0 = 0$, (17) yields $\mathcal{P}_h(\mathrm{e}^{j\cdot 0\cdot T_s^{\prime}}) = \sqrt{\left\|1-\Gamma_0^*(0)\right\|^2 + \sum_{k=1}^{F-1}\left\|\Gamma_k^*(0)\right\|^2}$. Based on the definition in (16) as well as the expressions of $P_d(z)$ and $P_{dh}(z)$, we get $\Gamma_k^*(0) = 1$ when $k = 0$ (by applying L'Hospital's Rule twice), and $\Gamma_k^*(0) = 0$ when $k \neq 0$. Therefore, $\mathcal{P}_h(\mathrm{e}^{j\cdot 0\cdot T_s^{\prime}}) = 0(<1)$.

Next consider the case of $\Omega_o = \Omega_N = \pi/T_s$. Evaluating the frequency responses of $P_d(z)$, $P_{dh}(z)$, and $H(z)$ in (14) yields

$$\Gamma_0^*(\Omega_N) = \frac{8\mathrm{e}^{j\pi/F}(\mathrm{e}^{j\pi/F}+1)}{F^3[\mathrm{e}^{j\pi/F}-1]^3(\mathrm{e}^{j\pi}+1)}. \tag{22}$$

For $F \geqslant 2$, $\Gamma_0^*(\Omega_N) \to \infty$ since $\mathrm{e}^{j\pi}+1 = 0$. Hence, in (17), $\mathcal{P}_h(\mathrm{e}^{j\Omega_N T_s^{\prime}}) \to \infty > 1$.

With $\mathcal{P}_h(\mathrm{e}^{j\cdot 0\cdot T_s^{\prime}}) < 1$ and $\mathcal{P}_h(\mathrm{e}^{j\Omega_N T_s^{\prime}}) > 1$, we thus have $B_p < \Omega_N$ based on a continuity analysis. ■

REFERENCES

[1] T. Atsumi and W. C. Messner, "Compensating for zoh-induced residual vibrations in head-positioning control of hard disk drives," *IEEE/ASME Transactions on Mechatronics*, vol. 19, no. 1, pp. 258–268, Feb 2014.

[2] Q.-W. Jia, "Intersample ripple-free multirate control with application to a hard disk drive servo," *IEEE/ASME Transactions on Mechatronics*, vol. 10, no. 3, pp. 341–345, June 2005.

[3] S. Berumen, F. Bechmann, S. Lindner, J.-P. Kruth, and T. Craeghs, "Quality control of laser- and powder bed-based Additive Manufacturing (AM) technologies," *Physics Procedia*, 2010.

[4] W. E. Frazier, "Metal additive manufacturing: A review," *J. Mater. Eng. Perform.*, vol. 23, no. 6, pp. 1917–1928, 2014.

[5] J. Tani, S. Mishra, and J. T. Wen, "Identification of fast-rate systems using slow-rate image sensor measurements," *IEEE/ASME Transactions on Mechatronics*, vol. 19, no. 4, pp. 1343–1351, Aug 2014.

[6] Y. C. Chang, B. Berry-Pusey, R. Yasin, N. Vu, B. Maraglia, A. X. Chatziioannou, and T. C. Tsao, "An automated mouse tail vascular access system by vision and pressure feedback," *IEEE/ASME Transactions on Mechatronics*, vol. 20, no. 4, pp. 1616–1623, Aug 2015.

[7] Y. Yamamoto and P. Khargonekar, "Frequency response of sampled-data systems," *IEEE Transactions on Automatic Control*, vol. 41, no. 2, pp. 166–176, 1996.

[8] M. Araki, Y. Ito, and T. Hagiwara, "Frequency response of sampled-data systems," *Automatica*, vol. 32, no. 4, pp. 483 – 497, 1996.

[9] T. Hagiwara, M. Suyama, and M. Araki, "Upper and lower bounds of the frequency response gain of sampled-data systems," *Automatica*, vol. 37, no. 9, pp. 1363 – 1370, 2001.

[10] Y. Yamamoto and M. Araki, "Frequency responses for sampled-data systems – their equivalence and relationships," *Linear Algebra and its Applications*, vol. 205-206, pp. 1319–1339, 1994.

[11] G. C. Goodwin and M. Salgado, "Frequency domain sensitivity functions for continuous time systems under sampled data control," *Automatica*, vol. 30, no. 8, pp. 1263–1270, 1994.

[12] J. S. Freudenberg, R. H. Middleton, and J. H. Braslavsky, "Inherent design limitations for linear sampled-data feedback systems," *International Journal of Control*, vol. 61, no. 6, pp. 1387–1421, 1995.

[13] O. Lindgarde and B. Lennartson, "Performance and robust frequency response for multirate sampled-data systems," in *American Control Conference, 1997. Proceedings of the 1997*, vol. 6. IEEE, 1997, pp. 3877–3881.

[14] M. W. Cantoni and K. Glover, "Frequency-domain analysis of linear periodic operators with application to sampled-data control design," *Proceedings of IEEE Conference on Decision and Control*, vol. 5, pp. 4318–4323 vol.5, 1997.

[15] T. Oomen, M. van de Wal, and O. Bosgra, "Design framework for high-performance optimal sampled-data control with application to a wafer stage," *International Journal of Control*, vol. 80, no. 6, pp. 919–934, 2007.

[16] O. Lindgärde, *Frequency analysis of sampled-data systems applied to a lime slaking process.* Chalmers University of Technology,, 1999.

[17] D. Wang, M. Tomizuka, and X. Chen, "Spectral distribution and implications of feedback regulation beyond nyquist frequency," in *Flexible Automation (ISFA), International Symposium on.* IEEE, 2016, pp. 23–30.

[18] R. E. Kalman, Y. C. Ho, and K. S. Narendra, "Controllability of linear dynamical systems," *Contributions to differential equations*, vol. 1, no. 2, pp. 189–213, 1963.

[19] B. A. Francis and T. Georgiou, "Stability theory for linear time-invariant plants with periodic digital controllers," *IEEE Transactions on Automatic Control*, vol. 33, no. 9, pp. 820–832, 1988.

[20] R. Middleton and J. Freudenberg, "Non-pathological sampling for generalized sampled-data hold functions," *Automatica*, vol. 31, no. 2, pp. 315 – 319, 1995.

[21] M. Hayes, *Statistical digital signal processing and modeling.* Wiley-India, 2009.

[22] K. J. Astrom and B. Wittenmark, *Computer-Controlled Systems: Theory and Design*, 3rd ed. Upper Saddle River, N.J: Prentice Hall, Nov. 1996.

[23] X. Chen and M. Tomizuka, "A minimum parameter adaptive approach for rejecting multiple narrow-band disturbances with application to hard disk drives," *IEEE Transactions on Control Systems Technology*, vol. 20, no. 2, pp. 408–415, March 2012.

[24] K. Astrom, P. Hagander, and J. Sternby, "Zeros of sampled systems," *Automatica*, vol. 20, no. 1, pp. 31 – 38, 1984.

[25] A. Al Mamun, G. Guo, and C. Bi, *Hard disk drive: mechatronics and control.* CRC Press, Taylor & Francis Group, London, 2007.

[26] I. D. Landau, A. C. Silva, T.-B. Airimitoaie, G. Buche, and M. Noe, "Benchmark on adaptive regulationï£¡ï£¡rejection of unknown/time-varying multiple narrow band disturbances," *European Journal of Control*, vol. 19, no. 4, pp. 237 – 252, 2013.

[27] L. Sievers and A. von Flotow, "Comparison and extensions of control methods for narrow-band disturbance rejection," *IEEE Transactions on Signal Processing*, vol. 40, no. 10, pp. 2377–2391, 1992.

[28] X. Chen and H. Xiao, "Multirate forward-model disturbance observer for feedback regulation beyond Nyquist frequency," *Systems & Control Letters*, vol. 94, pp. 181–188, August 2016.

[29] H. Fujioka and S. Hara, "Output regulation for sampled-data feedback control systems: Internal model principle and H_∞ servo controller synthesis," *Journal of the Chinese Institute of Engineers*, vol. 33, no. 3, pp. 335–346, Mar. 2011.

[30] T. Chen and B. A. Francis, "H_2-optimal sampled-data control," *IEEE Transactions on Automatic Control*, vol. 36, no. 4, pp. 387–397, Apr. 1991.

[31] R. Ravi, P. P. Khargonekar, K. D. Minto, and C. N. Nett, "Controller parametrization for time-varying multirate plants," *Automatic Control, IEEE Transactions on*, vol. 35, no. 11, pp. 1259–1262, Nov. 1990.

[32] S. Lall and G. Dullerud, "An LMI solution to the robust synthesis problem for multi-rate sampled-data systems," *Automatica*, vol. 37, no. 12, pp. 1909–1922, Dec. 2001.

[33] X. Jing and Z. Lang, *Frequency domain analysis and design of nonlinear systems based on Volterra series expansion: a parametric characteristic approach.* Springer, 2015.

[34] Z. Q. Lang, S. A. Billings, R. Yue, and J. Li, "Output frequency response function of nonlinear volterra systems," *Automatica*, vol. 43, no. 5, pp. 805–816, 2007.

[35] Z. Xiao and X. Jing, "Frequency-domain analysis and design of linear feedback of nonlinear systems and applications in vehicle suspensions," *IEEE/ASME transactions on mechatronics*, vol. 21, no. 1, pp. 506–517, 2016.

[36] I. S. Gradshtein, *Table of Integrals, Series, and Products.* Academic Press, Jan 1980, vol. 1.

[37] E. C. Titchmarsh and D. R. Heath-Brown, *The theory of the Riemann zeta-function.* Oxford University Press, 1986.

[38] H. Edwards, *Riemann's zeta function*, ser. Pure and Applied Mathematics. Elsevier Science, 1974.

[39] J. Sondow and E. W. Weisstein, "Riemann zeta function," from MathWorld–A Wolfram Web Resource. http://mathworld.wolfram.com/RiemannZetaFunction.html, accessed Dec. 5 2016.